Deciphering Spin-Activity Relationship of FeN_4 Moieties Bridged in Halogenated MXenes for Oxygen Reduction

*Shuren Zhang, Genban Sun **

AUTHOR ADDRESS. Beijing Key Laboratory of Energy Conversion and Storage Materials Institution, College of Chemistry, Beijing Normal University, Beijing 100875, China

ABSTRACT: Spin control of FeN_4 moieties is critical for enhancing the electrocatalytic oxygen reduction reaction (ORR). The relationship between Fe-N_4 spin state transitions and ORR activity is complex and remains controversial due to discrepancies between theoretical models and experimental catalyst structures, along with potential misinterpreting characterization data. In this study, we utilized Ti3C2Tx MXenes with various terminations (−I, −Br, −Cl, −F, and −O), integrated with iron phthalocyanine (FePc), to form model catalysts with defined FeN_4-T_x-Ti structures, allowing for precise modulation of the FeN_4 spin states and establishing a clear correlation between the intermediate spin state and improved ORR performance. Specifically, $Ti_3C_2Br_x$/FePc, featuring 88.1% intermediate spin state, exhibited superior electrochemical performances, with an ORR half-wave potential of 0.94 V versus RHE, and doubled power densities in Zn-air batteries (252.5 mW cm^{-2}) and H_2-O_2 fuel cells (350.7 mW cm^{-2}) compared to FePc with 17.1% intermediate spin state. Theoretical studies confirmed that the intermediate spin state leads to electron filling in the anti-bonding orbital composed of Fe $3dz^2$ and O_2 π^* orbitals, significantly improving O_2 activation and ORR activity. This research advances our understanding of the spin-related origins of catalytic activity and sets the stage for the design and optimization of advanced ORR catalysts.

Introduction

Fuel cell and rechargeable metal-air batteries represent a leap forward in clean energy technology, offering a more efficient and environmentally benign alternative to conventional combustion engines[1-3]. However, their widespread adoption faces a significant challenge: the oxygen reduction reaction (ORR) at the cathode is markedly slower than the hydrogen oxidation at the anode, limiting the overall performance of fuel cells and metal-air batteries[4]. Platinum-group metals (PGMs) have long been the gold standard for ORR catalysts due to their high catalytic activity[5, 6]. Yet, their scarcity and high cost pose substantial barriers to widespread use[7]. This challenge has directed research attention towards iron-nitrogen-carbon (Fe-N-C) catalysts in the past decade, given their potential to serve as viable alternatives to PGMs in fuel cells and metal-air batteries[8]. Substantial research efforts have confirmed that the FeN_4 moieties acts as the principal active site within Fe-N-C catalysts, facilitating the ORR[9-11]. Remarkable advancements in modifying the FeN_4 moieties and boosting the inherent activity of Fe-N-C composites have been achieved, for example, through altering the metal center[12], adjusting coordination arrangements[13], introducing morphological changes[14], and creating atomic vacancies[15] and edge defects[16]. Among these strategies, triggering spin state transitions stands out as a highly targeted approach for adjusting the electronic structure, significantly improving both the catalytic performance and stability[17]. For example, Wang et al. suggested that maintaining FeN_4 moieties in a low spin state could balance the energy needed for adsorbing and releasing reaction intermediates, thereby enhancing ORR efficiency[18]. Zhang and Wang et al. argued that transitioning from a low to a medium spin state improves the filling of Fe's e_g orbitals, facilitating interaction with oxygen's antibonding π-orbital and increasing oxygen affinity, which in turn boosts ORR activity[3, 19]. Additionally, some researchers believe that a high spin state at $Fe\text{-}N_4$ moieties can enhance oxygen adsorption, further optimizing ORR performance[20, 21]. Despite the groundwork established by pioneering research, the precise relationship between electronic spin state transitions and ORR activity is still elusive an controversial. This is largely due to the divergence between theoretical models and the actual structures of catalysts in practice, as well as inappropriate interpretation of characterization data results, such as magnetic susceptibility[22]. Therefore, it is crucial to align theoretical models with actual catalyst structures and interpret data accurately to uncover the relationship between electronic spin state transitions and ORR activity, enabling the rational design of high-performance ORR catalysts.

MXene, with its customizable surface terminations through the choice of etching agent used in their preparation, provides precise axial coordination to the Fe-N_4 moieties, suggesting its remarkable potential as a platform for in-depth investigation of the relationships between electronic spin states and activity[23]. Herein, $Ti_3C_2T_x$ MXenes with various terminations (-I, -Br, -Cl, -F, -O) were synthesized and integrated with iron phthalocyanine (FePc), which contain the typical FeN_4 moieties, to build the FeN_4-T_x-Ti structures within $Ti_3C_2T_x$/FePc composites.

The composite $Ti_3C_2T_x$/FePc, selected as a model catalyst, possesses FeN_4-T_x-Ti (Tx = -I, -Br, -Cl, -F, -O) structures, as confirmed by X-ray absorption spectroscopy (XAS). The spin state was determined using ^{57}Fe Mössbauer spectroscopy and temperature-dependent magnetization (M-T) measurements. Our systematic evaluation revealed a strong positive correlation between the ORR performance and both the intermediate spin proportion and the effective single electron numbers. Through density functional theory (DFT), we showed that $Ti_3C_2Br_x$/FePc, in the intermediate spin state, promotes a hybridization of Fe $3dz^2$ and O_2 π^* orbitals across the Fermi level, leading to electron filling in the anti-bonding orbital composed of Fe $3dz^2$ and O_2 π^* orbitals, significantly improving O_2 activation efficiency compared to FePc, where such electron filling is absent.This work unravels the spin-activity relationship in ORR and provides fundamental significance of the electron spin state of FeN_4 moieties in the regulation of the ORR catalytic activity, offering reference frames for the engineering of high-performance ORR catalysts in electrochemical energy technologies.

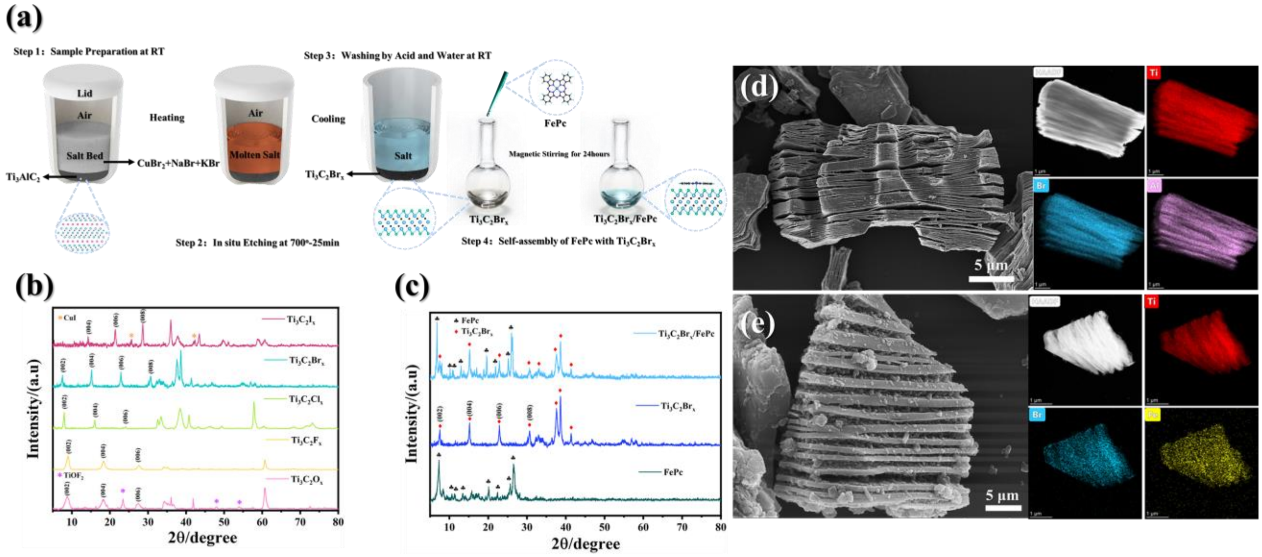

Figure. 1 (a) Schematic illustration of the synthesis of $Ti_3C_2Br_x$ and $Ti_3C_2Br_x$/FePc**; (b)** Full-scale X-ray diffraction (XRD) patterns of MXenes obtained in the present work； **(c)** XRD patterns of $Ti_3C_2Cl_x$/FePc, $Ti_3C_2F_x$, and pristine FePc; **(d-e)** SEM and HAADF-STEM images of **(d)**$Ti_3C_2Br_x$ and **(e)**$Ti_3C_2Br_x$/FePc along with corresponding EDS mappings

Material Preparation and Characterization

As illustrated in Figure 1a, we initially synthesized MXenes with various terminal groups, subsequently employing a facile self-assembly process to fabricate the Ti3C2Tx/FePc model catalysts by mixing even dispersions of FePc with $Ti_3C_2T_x$ MXene in dimethylformamide (DMF) under magnetic stirring[9]. Lewis-acid etching techniques were utilized to introduce -I, -Br, and -Cl terminations[24-26], while conventional HF-based etching methods were applied to synthesize -F terminated Ti_3C_2 MXenes[9]. Notably, the synthesis and purification process inevitably led to the introduction of minor oxygen terminal groups in all prepared MXenes, prompting the specific synthesis of $Ti_3C_2O_x$ for a detailed investigation of its influence on the FeN_4 moieties' spin states, achieved by optimizing oxygen atom coverage on the surface through furnace treatment[27].

The XRD patterns of the halogenated $Ti_3C_2T_x$ MXenes were consistent with previous reports[23, 24, 28]. The XRD pattern of $Ti_3C_2O_x$, similar to $Ti_3C_2F_x$, displayed peaks associated with $Ti(OF)_2$, indicative of oxidation during the preparation process[19, 27], yet no TiO_2 phase was detected. After self-assembly with FePc, the XRD pattern of $Ti_3C_2T_x$/FePc composite indicated a composite of $Ti_3C_2T_x$ and FePc (Figure S1). SEM images of the pristine $Ti_3C_2T_x$ MXenes, including $Ti_3C_2O_x$, exhibited the characteristic accordion-like morphology with open laminae (Figure S2). The $Ti_3C_2T_x$/FePc composite preserved the layered structure of $Ti_3C_2T_x$, with an increased surface roughness, in agreement with previous studies (Figure S3).

Energy-dispersive X-ray spectroscopy (EDS) mapping confirmed the uniform distribution of titanium (Ti), carbon (C), and halogen elements in the MXene particles, with halogen elements uniformly distributed due to the effective leaching in Lewis acid salts and HF solution[23, 28] (Figure S1d & Figure S2). The elemental compositions obtained from EDS analyses of these halogenated MXenes are thoroughly documented in Table S2. Notably, the atomic ratio of Ti to Br was approximately 3:2, suggesting a nearly complete coverage of Br atoms on the surface terminals[23, 29]. The Ti:O ratio in halogenated MXenes was significantly lower than that of Ti and halogen elements, implying minor oxygen occupancy at the surface. Following the oxidation procedure, $Ti_3C_2O_x$ exhibited a Ti:O ratio of 3:2.1, implying a nearly full oxygen coverage on the surface. Additionally, a comparison of the elemental compositions across different halogenated MXenes revealed a significant reduction in the Ti to Al atomic ratio in all samples, confirming the selective removal of the Al layer. The Fe content within the $Ti_3C_2T_x$/FePc composites, determined via inductively coupled plasma mass spectrometry (ICP-MS), revealed that $Ti_3C_2Br_x$/FePc had a Fe loading of ca. 5.07%, comparable to other $Ti_3C_2T_x$/FePc composites (Table S3).

The surface composition and chemical state of the prepared $Ti_3C_2T_x$ and $Ti_3C_2T_x$/FePc composites were further elucidated through X-ray photoelectron spectroscopy (XPS) analysis (Figure S4-S8). The Ti 2p spectrum of the synthesized halogenated MXenes, after deconvolution, exhibited distinct peaks corresponding to Ti–I, Ti–Br, Ti–Cl, and Ti–F chemical bonds at peak positions of 457.8, 458.3, 458.5, and 456.7 eV, respectively, ascribing these peaks to the respective -I, -Br, -Cl, and -F surface functional groups[23, 25, 28-30]. The I 3d, Br 3d, Cl 2p, and F 1s spectra corroborated the existence of these Ti–T_x bonds. The detection of Ti–O bonds attested to the presence of oxygen surface terminations, a result of the partial surface oxidation during synthesis and the ammonium persulfate (APS) acid-washing process[26, 30]. In $Ti_3C_2O_x$, as shown in Figure S7, the F 1s spectrum exhibited a notable decrease in F 1s peak intensity, with the Ti–O peak becoming dominant in the Ti 2p spectrum, indicating substantial oxygen coverage, corroborated by EDS analysis and previous literatures[19, 27]. In the high-resolution XPS spectra of the $Ti_3C_2T_x$/FePc samples, peaks indicative of Fe-T_x (Tx = Br, Cl, F, O) coordination were observed in the respective Br 3d, Cl 2p, F 1s, and O 1s high-resolution spectra, with the exception of $Ti_3C_2I_x$/FePc (Figure S4-S8). In the $Ti_3C_2I_x$/FePc sample, the integration of FePc led to a noticeable reduction in the intensity of I 3d peaks (Figure S8), suggesting the instability of iodine terminations on Ti_3C_2 MXenes, attributed to the relatively weak bonding between the outermost titanium atoms and the iodine terminals, limiting the formation of FeN_4-I-Ti structure in the $Ti_3C_2I_x$/FePc sample[23, 25] Moreover, XPS spectral analysis of $Ti_3C_2T_x$/FePc further revealed the inductive effect of FeN_4-T_x-Ti structures on electronic redistribution, evidenced by positive shifts in the Fe 2p and Ti 2p peaks relative to FePc, and Ti_3C_2Tx, while negative shifts in Ti-T_x bonds, within the corresponding Br 3d, Cl 2p, F 1s, and O 1s high-resolution XPS spectrum peaks, due to their strong electronegativity (Figures S4-7&Tables S5-13).

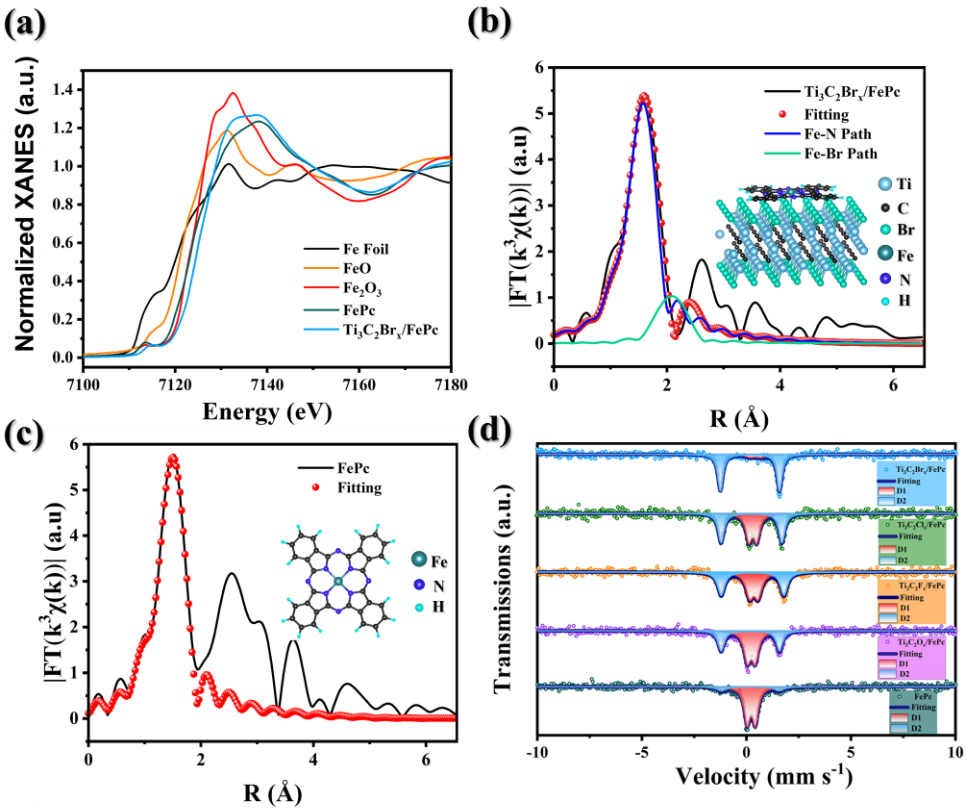

Figure 2. (a) XANES K-edge spectra of Fe foil, FeO, Fe_2O_3, FePc and $Ti_3C_2Br_x$/FePc; FT k^3-weighted Fe *K*-edge EXAFS spectra and the indicated structures of **(b)** $Ti_3C_2Br_x$/FePc and **(c)** FePc; **(d)** ^{57}Fe Mössbauer spectrum of $Ti_3C_2T_x$/FePc (T_x =Br, Cl, F, O) and FePc at 298 K.

Electronic States and Coordination Environment of FeN_4 moieties in $Ti_3C_2T_x$/FePc catalysts

To gain deeper insights into the local coordination geometry and electronic states, we turned to synchrotron X-ray absorption near-edge structure (XANES) and extended X-ray absorption fine structure (EXAFS) analyses (Figures 2a-c). These methods are particularly effective due to their strong sensitivity to the arrangement of absorbing atoms. The X-ray absorption near-edge structure (XANES) curves reveal that the absorption edge position of $Ti_3C_2Br_x$/FePc closely align with that of Fe_2O_3, suggesting the Fe species in $Ti_3C_2Br_x$/FePc are in an approximately +3 oxidation state (Figure 2a). This is further evidenced by a noticeable positive shift in the absorption edge compared to FePc, indicating changes in the electronic structure of the Fe atomic sites, which is corroborated by the Fe 2p XPS spectrum of $Ti_3C_2Br_x$/FePc (Figure S4b). Furthermore, the pre-edge peak at approximately 7114 eV, which is characteristic of the

1s→4pz electric dipole transition observed in FePc, exhibits reduced intensity in $Ti_3C_2Br_x$/FePc compared to that in FePc[20, 31]. This observation suggests a transition from the square-planar D4h symmetry to the tetragonal C4v symmetry, a transformation likely induced by the introduction of FeN_4-Br-Ti structure[19]. The Fourier-transformed (FT) k^3-weighted EXAFS spectra analysis for $Ti_3C_2Br_x$/FePc and FePc yields average coordination numbers of 4.9 and 3.9, as outlined in Table S14. Specifically, coordination numbers for Fe-N and Fe-Br bonds are identified as 4.1 and 0.8, respectively. This data illustrates that iron within $Ti_3C_2Br_x$/FePc engages with four nitrogen atoms from phthalocyanine (Pc) and a single axial Br ligand from $Ti_3C_2Br_x$, creating a five-coordinated structure. Five-coordinated structures are seen as potential catalytic sites because their unsaturated coordination allows oxygen intermediates to bind and transform into six-coordinated structures after the adsorption[32]. Combined with the XPS results previously discussed, we have confirmed the existence of our proposed FeN_4-T_x-Ti structure model.

^{57}Fe Mössbauer spectroscopy has been one of the most sensitive techniques in probing the Fe nucleus and distinguishing the spin states of similar FeN_4 environments but with different coordination structures[33-35]. Therefore, we conducted Mössbauer spectroscopy measurements on all the prepared $Ti_3C_2T_x$/FePc to provide deep insights into the tuning effect of FeN_4-T_x-Ti (T_x = Br, Cl, F, O) structures on the spin state of Fe(III)N_4 moieties and the relationship between variation of spin state and ORR performance of prepared catalysts, which will be discussed later in detail. As depicted in Figure 2d, the ^{57}Fe Mössbauer spectra of all the prepared $Ti_3C_2T_x$/FePc samples were deconvoluted and fitted well by two doublets: D1 and D2[19-21]. D1, with an isomer shift ranging from 0.23 to 0.43 mm s^{-1} and a quadrupole splitting from 0.38 to 0.64 mm s^{-1}, is identified as the Fe(III)-N_4 moieties in the low spin state. D2, having a similar isomer shift range as D1 but with a much larger quadrupole splitting value ranging from 2.52 to 3.00 mm/s, is attributed to the Fe(III)-N_4 moieties in intermediate spin state . After introducing $Ti_3C_2T_x$ (T_x = Br, Cl, F, O), D1's relative area decreases, and D2's relative area gradually increases from 17.1% to 88.1%, illustrating their varied tuning effect of FeN_4-T_x-Ti structures on transitioning from low spin to intermediate spin in Fe(III)-N_4 moieties (Figure 2d), owing to its different intrinsic ability to modulate the strength of the crystal field. Specifically, the FeN_4-Br-Ti structure almost entirely shifts the Fe(III)-N_4 from low spin to intermediate spin, evidenced by the dominant D2 peak with a relative area of 88.1%. This is attributed to its comparatively weaker field strength and the almost complete coverage of Br atoms at the surface terminal sites[20]. Notably, upon further examination of the $Ti_3C_2I_x$/FePc spin state, the D1 peak was predominantly observed, with a relative area of 98.6%, attributable to the limited formation of the FeN_4-I-Ti structure, which further substantiated the FeN_4-T_x-Ti structures' effectiveness in spin state control.

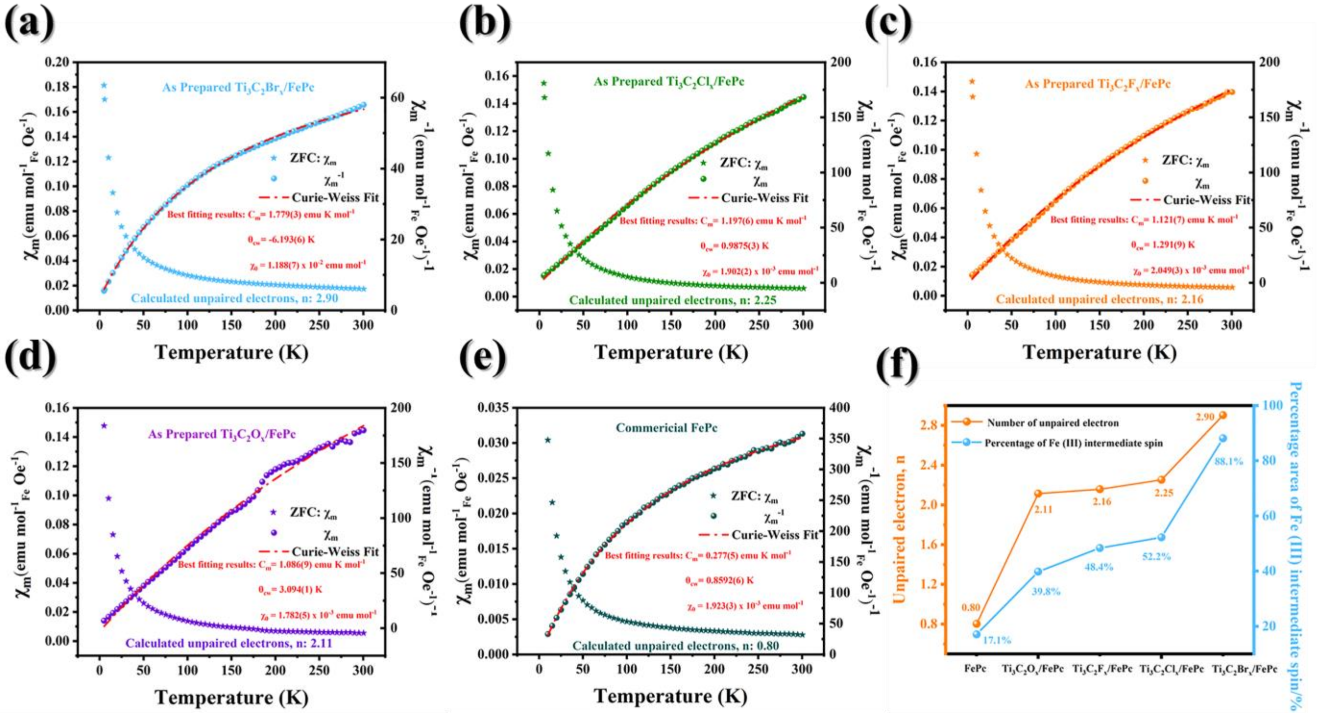

Figure 3. Temperature dependence of the magnetic susceptibility χ_m (left) and plots of χ_m^{-1} (right) vs *T* for **(a)** $Ti_3C_2Br_x$/FePc, **(b)**$Ti_3C_2Cl_x$/FePc, **(c)**$Ti_3C_2F_x$/FePc, **(d)**$Ti_3C_2O_x$/FePc and **(e)** pristine FePc with the best Curie−Weiss fitting results shown by red dashed lines; **(f)** Trend analysis of the number of unpaired electrons and the proportion of Fe (III) intermediate spin states across FePc and $Ti_3C_2T_x$/FePc composites (T_x = Br, Cl, F, O).

Given that the assignment of the Mössbauer spectroscopy signatures is not univocal due to many factors, including material synthesis method and reaction mechanisms, the most reliable interpretation of these spectra should be corroborated with data from other independent characterization techniques[34]. To this end, we employed zero-field cooling (ZFC) temperature-dependent magnetic susceptibility (M-T) measurements. This method's distinct capacity to assess a material's magnetic properties allowed us to quantify unpaired electrons and thereby determine the electron spin configuration[36].

It should be noted that many researchers often report inappropriate effective moments μ_{eff} arise from the misapplication of the Curie–Weiss equation (S1) by many researchers. This misapplication involves fitting susceptibility curves without incorporating the temperature-independent factor (χ_0), which accounts for core diamagnetism, Pauli paramagnetism, or van Vleck paramagnetism[22]. One can only fit plot χ_{mol}^{-1} vs. T to the Curie–Weiss equation S1 without considering temperature-independent factor (χ_0) if a strictly linear trend is observed. In practical terms, if the χ_{mol}^{-1} vs. T plot reveals positive or negative curvature, employing the modified Curie–Weiss equation (S2) is recommended[22]. By fitting the χ_{mol}^{-1} vs. T plots with the modified Curie–Weiss equation, we determined the effective magnetic moments (μ_{eff}) using equation (S3) to be 3.77, 3.09, 2.99, 2.94, and 1.50 μB for $Ti_3C_2Br_x$/FePc, $Ti_3C_2Cl_x$/FePc, $Ti_3C_2F_x$/FePc, $Ti_3C_2O_x$/FePc, and FePc, respectively. Following this, we calculated the number of unpaired electrons (n) using equation S4[9]. The calculated numbers of unpaired electrons for Ti_3C_2Brx/FePc, $Ti_3C_2Cl_x$/FePc, $Ti_3C_2F_x$/FePc, $Ti_3C_2O_x$/FePc, and FePc are 2.90, 2.25, 2.16, 2.11, and 0.80, respectively (Figure 3f), aligning well with the Mössbauer spectroscopy findings. As shown in Figure 3f, there's a clear correlation and similarity between the trends in variation of single electron numbers from M-T measurements and D2's intermediate spin relative proportions in Mössbauer spectra. This consistency validates the peak assignments in the Mössbauer spectra, further endorsing the impactful role of FeN_4-T_x-Ti structures in regulating the spin state of Fe 3d electrons from low to intermediate spin at varying degrees due to their intrinsic unique crystal field strength.

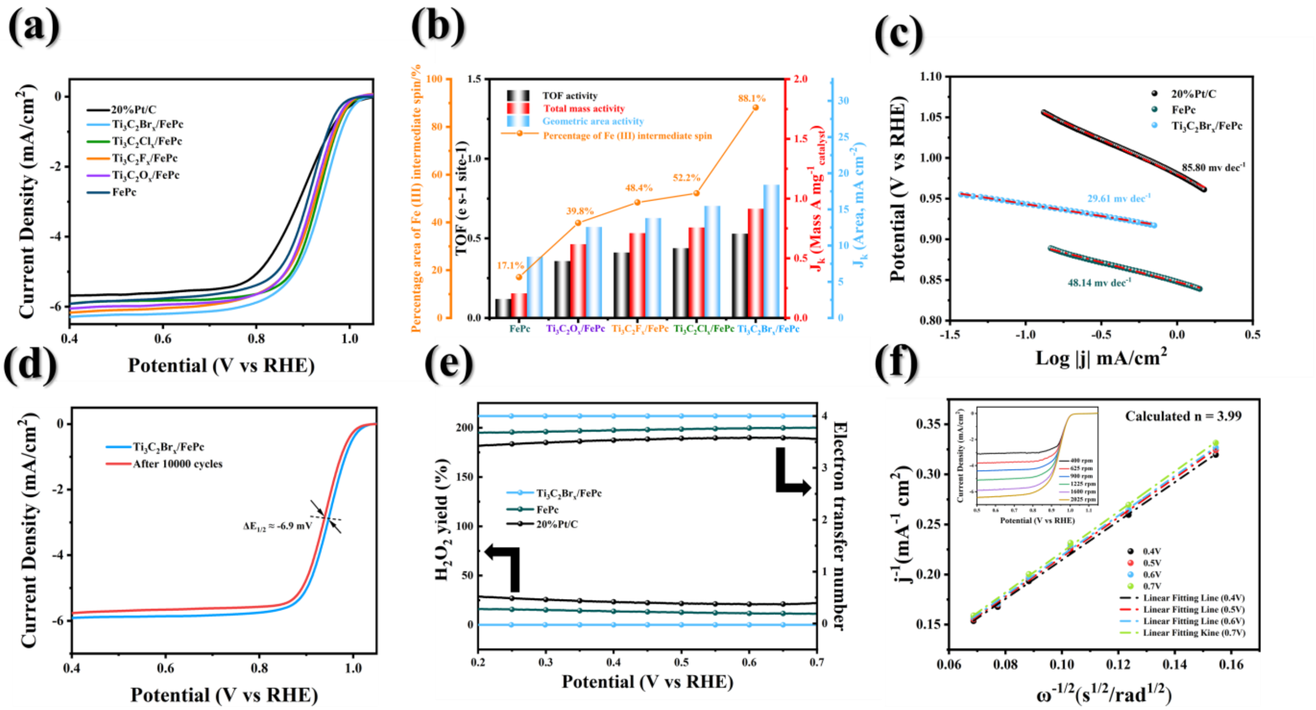

Figure 4. (a) Steady-state ORR polarization plots of FePc and $Ti_3C_2T_x$/FePc (T_x = Br, Cl, F, O) performed in 0.1 M KOH at room temperature with a rotation rate of 1600 rpm; **(b)** Comparative analysis of Fe (III) intermediate spin state proportions at 298K, kinetic current densities, and turnover frequencies at 0.90 V vs. RHE for ORR across FePc and $Ti_3C_2T_x$/FePc (Tx = Br, Cl, F, O) catalysts; **(c)** Tafel slopes of 20% Pt/C, FePc and $Ti_3C_2Br_x$/FePc, **(d)** Steady-state ORR polarization plots before and after the 10000 potential cycling for the $Ti_3C_2Br_x$/FePc; **(e)** H_2O_2 yield and electron transfer numbers of 20% Pt/C, FePc and $Ti_3C_2Br_x$/FePc;**(f)** Koutecky–Levich plots of $Ti_3C_2Br_x$/FePc at +0.4, +0.5, +0.6 and +0.7 V *vs*. RHE. Inset shows the steady-state ORR curves at different rotation rates of 400, 625, 900, 1225, 1600 and 2025 rpm.

Spin State Dependent Electrocatalytic Activities of ORR

Building on our magnetic susceptibility and Mössbauer spectroscopy findings, we evaluated the oxygen reduction reaction (ORR) activity of electrodes crafted from as-prepared $Ti_3C_2T_x$/FePc (T_x = Br, Cl, F, O) and FePc in a 0.1 mol L^{-1} KOH electrolyte, as shown in Figure 4a. Our steady-state ORR polarization measurements revealed a direct correlation between the enhancement in ORR performance metrics—including half-wave potential ($E_{1/2}$), geometric activity (J_k), mass activity (J_m), and turnover frequency

(TOF) at 0.90 V versus RHE—and the increase in the percentage of Fe(III)'s intermediate spin state, as determined from Mössbauer spectroscopy (Figure 4b). Remarkably, $Ti_3C_2Br_x$/FePc distinguishes itself with the highest half-wave potential ($E_{1/2}$) of 0.94 V versus RHE among all synthesized $Ti_3C_2T_x$/FePc and FePc catalysts, and it achieves a kinetic current density of 17.28 mA cm^{-2}, significantly surpassing FePc (8.47 mA cm^{-2}) and Pt/C (0.71 mA cm^{-2}) by factors of 2.04 and 24.3, respectively. Moreover, the mass activity (J_m) and the turnover frequency (TOF) at 0.9 V for $Ti_3C_2Br_x$/FePc were determined to be 859.6 mA $mg_{catalyst}^{-1}$ and 0.497 e s^{-1} $site^{-1}$, respectively, significantly outperforming FePc (206.95 mA $mg_{catalyst}^{-1}$ and 0.119 e s^{-1} $site^{-1}$) and Pt/C (9.69 mA mg_{Pt}^{-1} and 0.0196 e s^{-1} $site^{-1}$). Additionally, $Ti_3C_2I_x$/FePc, predominantly in the low spin state (98.6%), exhibited ORR activity slightly lower than that of FePc (Figure S10b). These findings definitively illustrate that ORR performance enhancement is closely tied to the intermediate spin state of Fe(III)N_4 moieties, suggesting the key role of transitioning from low to intermediate spin state in optimizing electrocatalytic activity. We further reveal that $Ti_3C_2Br_x$/FePc exhibits an outstanding Tafel slope of 29.61 mV dec^{-1}, significantly lower than those observed for FePc (48.14 mV dec^{-1}) and Pt/C (85.80 mV dec^{-1}), indicating accelerated ORR kinetics as presented in Figure 4c.

Electrocatalyst durability is crucial for real-world applications. We evaluated the durability of $Ti_3C_2Br_x$/FePc for ORR using accelerated tests, as shown in Figure 4d. After 10,000 cycles between 0.6 and 1.1 V vs RHE, the half-wave potential of Ti3C2Brx/FePc decreased by only -7 mV, significantly outperforming pure FePc (-15.3 mV) and commercial Pt/C (-67.7 mV), demonstrating the exceptional durability of Ti_3C_2Brx/FePc in ORR applications (Figure S11a-b).

The electron transfer number (n), pivotal in defining the ORR pathway and consequently the application scenario, was examined using staircase voltammetry (SCV) across various rotating rates, alongside the corresponding Koutecky-Levich plot (Figure 4f). The findings reveal that $Ti_3C_2Br_x$/FePc closely approaches a four-electron transfer pathway, with an electron transfer number (n) of approximately 3.99, outperforming that of FePc ($n \approx 3.91$) and Pt/C ($n \approx 3.85$), with the corresponding hydrogen peroxide yield below 0.4% suggesting that the Ti_3C_2Brx/FePc's high selectivity in the four-electron process in ORR (Figure 4e). Investigating the ORR performance of Ti3C2Brx/FePc catalysts with varying weight ratios revealed that a 1:1 M-TiN to FePc ratio optimally boosts synergetic effects, resulting in the highest ORR activity (Figure S11c).

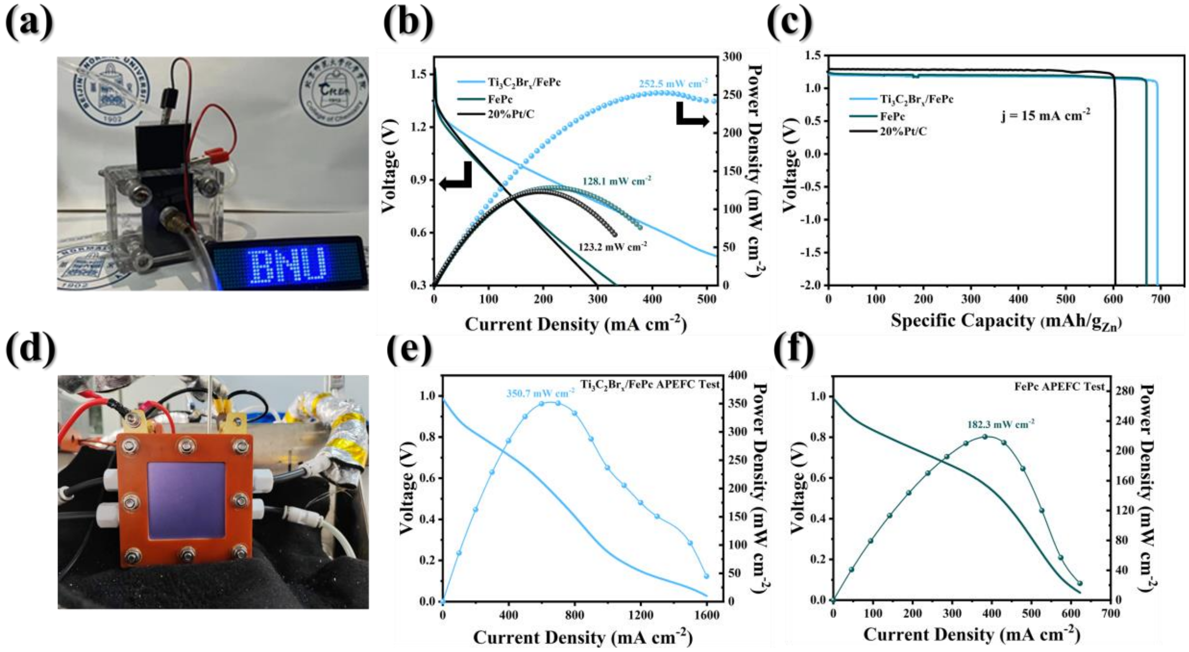

Figure 5. (a) Photograph of a 'BNU' Light-emitting diode panel powered by a single Zn-Air Battery assembled with the $Ti_3C_2Br_x$/FePc catalyst; **(b)** Polarization and power density curves of Zn-air batteries using $Ti_3C_2Br_x$/FePc, FePc, and 20% Pt/C as cathodic catalysts;**(c)** specific capacity of Zn-air using $Ti_3C_2Br_x$/FePc, 20%Pt/C, and FePc as cathodic catalysts; **(d)** Photograph of H_2/O_2 AEMFC; **(e-f)** H_2-O_2 AEMFC polarization and power density curves of $Ti_3C_2Br_x$/FePc and FePc, respectively. The catalyst loading was maintained at 0.4 mg_{Pt} cm^{-2} and 4 $mg_{catalyst}$ cm^{-2} for the anode and cathode, respectively; Fuel cell operating conditions: temperature = 60 °C, backpressure of gas = 0.125 MPa and 0.25 MPa for anode and cathode side of the cell, respectively. Fully humidified H_2 and O_2 were fed at a flow rate 0.5 L/min and 1L/min, respectively;

Encouraged by the exceptional ORR performance, our investigation extended to evaluating $Ti_3C_2Br_x$/FePc as an electrocatalyst within a homemade Zn-air battery (ZAB) (Figure 5a). We benchmarked its performance against that of FePc and commercial Pt/C in ZABs assembled under the same conditions. $Ti_3C_2Br_x$/FePc achieved a peak power density of 252.5 mW cm^{-2}, roughly double that of FePc (128.1 mW cm^{-2}) and 20% Pt/C (123.2 mW cm^{-2}) shown in Figure 5b. Moreover, the open-circuit voltage (OCV) for the ZAB incorporating $Ti_3C_2Br_x$/FePc reached 1.51 V, surpassing those with FePc (1.49 V) and 20% Pt/C (1.48 V) as shown in Figure S12. Additionally, the $Ti_3C_2Br_x$/FePc-based ZAB exhibited a discharge-specific capacity of 692.9 mAh/g_{Zn} at 15 mA cm^{-2}, exceeding the performance of ZABs with FePc and 20% Pt/C (Figure 5c). Impressively, $Ti_3C_2Br_x$/FePc also powered a "BNU" LED panel, underscoring its capability for portable energy devices, as shown in Figure 5a.

We further constructed an anion exchange membrane fuel cell (AEMFC) membrane electrode assembly (MEA) utilizing $Ti_3C_2Br_x$/FePc and FePc as the cathode catalysts, respectively (Figure 5d & Figure S13). Demonstrated in Figure 5e and f, the MEA with $Ti_3C_2Br_x$/FePc achieved a peak power density of 350.7 mW cm^{-2} in a H_2-O_2 cell, nearly doubling the power density of the MEA with FePc (182.3 mW cm^{-2}). This showcases the significant impact of modulating spin states on enhancing performance in practical energy applications.

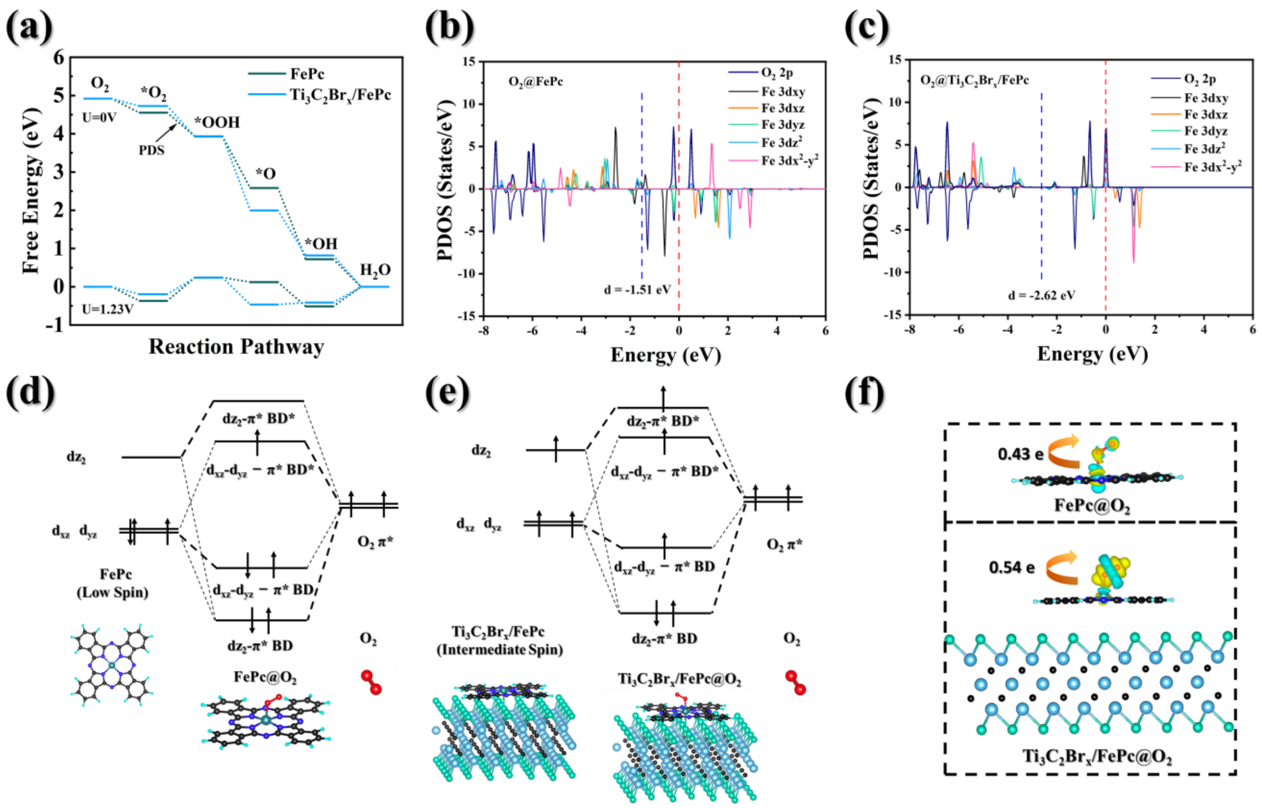

Figure 6. (a) Free energy diagrams of ORR pathways on $Ti_3C_2Br_x$/FePc and FePc; **(b-c)** The projected density of states of O_2* adsorption on **(b)** FePc and **(c)** $Ti_3C_2Br_x$/FePc; **(d-e)** Orbital interactions of **(e)** FePc@O_2 and **(f)** $Ti_3C_2Br_x$/FePc@O_2 (major interaction between Fe3dxz, dyz, dz^2 and O_2 π* orbitals). The dashed lines indicate the major components from fragments in each bonding (BD) or antibonding (BD*) orbital. **(f)** The charge density differences of the O_2 adsorption on FePc and $Ti_3C_2Br_x$/FePc. The isosurface level set to 0.008 e $Å^{-3}$, the yellow and cyan stands for electron accumulation and depletion area, respectively

ORR Activity origin for FeN_4 moieties with intermediate spin

To better understand the origin of intermediate spin Fe(III) in $Ti_3C_2Br_x$/FePc catalysts and its correlation with the electronic spin state and ORR activity at Fe(III)N_4 moieties, DFT calculations were performed. By constructing $Ti_3C_2Br_x$/FePc models grounded in XAFS structural analysis, we achieved the most accurate approximation of the actual catalyst, thus minimizing oversimplification and enhancing the accuracy of our reaction mechanism insights from DFT simulations.

ORR processes with four-electron transfers on $Ti_3C_2Br_x$/FePc and FePc were modeled and analyzed. At a potential of 1.23 V, as shown in Figure 6a, the free energy differences, particularly for the endothermic steps, were determined. The O_2 activation step presented the largest free energy difference, marking it as the potential-determining step (PDS) for both FePc and $Ti_3C_2Br_x$/FePc. Therefore, enhancing O_2 activation could reduce the energy barrier for *OOH formation, thereby increasing ORR activity. The determined overpotentials for ORR on FePc and $Ti_3C_2Br_x$ were determined to be 0.61 V and 0.43 V, respectively, indicating $Ti_3C_2Br_x$/FePc's superior ORR performance compared to FePc.

To further elucidate the electronic structure and O_2 activation mechanism, we computed the projected densities of states (PDOS) for O_2 adsorbed on $Ti_3C_2Br_x$/FePc and FePc (Figure 6b-c). Initially, we calculated the d-band center for both $Ti_3C_2Br_x$/FePc@O_2 and FePc@O_2. According to d-band center theory, catalysts with d-band centers further from the Fermi energy level exhibit weaker adsorption for adsorbates[37], and lowering the d-band center is crucial for enhancing ORR activity by facilitating effective attachment and detachment of reactants[38]. Our assessment revealed that the d-band center of $Ti_3C_2Br_x$/FePc@O_2 is positioned at −2.62 eV, further from the Fermi level compared to FePc@O_2 at −1.51 eV, leading to a reduced adsorption energy barrier for O_2 on $Ti_3C_2Br_x$/FePc (0.19 eV) versus FePc (0.37 eV) (Figure 6a). Given that O_2 activation is the rate-determining step (RDS) for ORR on $Ti_3C_2Br_x$/FePc, we further explored the interaction strength between O_2 and the Fe(III)N_4 moieties in both catalysts. In the case of FePc, O_2 adsorption positioned the hybrid orbitals of Fe's $3dz^2$ and O_2's π^* above the Fermi level (Figure 6b). In contrast, for $Ti_3C_2Br_x$/FePc, the hybridization between O_2 π^* and Fe $3dz^2$ orbitals occurred across the Fermi level, indicating superior electrical conductivity and facilitating rapid electron transfer to enhance O_2 activation and ORR performance (Figure 6c)[39].

Building on these analyses, we constructed schematic frontier orbital diagrams to depict the orbital interactions of $Ti_3C_2Br_x$/FePc and FePc with oxygen (Figure 6d-e). These diagrams illustrate that the primary interactions involve the Fe 3dxz, 3dyz, and 3dz^2 orbitals of and the π* orbitals of O_2[32], since the 3dxy and 3dx^2-y^2 orbitals of Fe(III)N_4 with other orbitals of adsorbed O_2 are considered negligible due to symmetry conservation[35]. The intermediate spin state in $Ti_3C_2Br_x$/FePc results in electron filling in the anti-bonding orbital composed of Fe 3dz^2 and O^2 π* orbitals, leading to more efficient O_2 activation compared to FePc, where no electron filling occurs in the anti-bonding orbital.

To validate our reasoning, charge density difference and Bader charge analysis were performed, showing that electron transfers to adsorbed O_2 were 0.43 e for FePc and 0.54 e for $Ti_3C_2Br_x$/FePc (Figure 6f). This analysis clearly demonstrates the more efficient charge transfer in $Ti_3C_2Br_x$/FePc, further supporting the enhanced ORR performance due to optimized O_2 activation in the intermediate spin state.

Although both experimental and theoretical results underscore the pivotal role of transitioning from low to intermediate spin states at Fe(III)N_4 moieties in enhancing ORR activity, the high spin state of Fe(III)N_4 has not yet been thoroughly examined. Nevertheless, based on current analyses and existing literature, it is plausible to infer that a high spin state of Fe(III)N_4 would lead to inferior ORR activity. This inference is grounded in symmetry conservation, which dictates that interactions between the dx^2–y^2 and dxy orbitals of Fe 3d and the orbitals of oxygenated adsorbed intermediates are minimal[32]. Consequently, changes in the occupancy of the Fe 3dx^2–y^2 or dxy orbitals are unlikely to significantly impact O_2 activation or decrease the energy barrier for the ORR reaction. Furthermore, a high spin state in Fe(III)N_4 is expected to further disrupt the degeneracy of its electronic states and lower the d-band center, resulting in excessively weak O_2 adsorption affinity and compromised ORR performance[37, 38].

Conclusions

In conclusion, our research has successfully demonstrated the critical influence of spin state control in Fe(III)N_4 moieties on the electrocatalytic performance of the oxygen reduction reaction (ORR). By employing $Ti_3C_2T_x$ MXenes with various terminations, specifically $Ti_3C_2Br_x$, integrated with iron phthalocyanine (FePc), we synthesized catalysts with well-defined FeN_4-T_x-Ti structures. Our results show a significant enhancement in ORR activity correlated with the intermediate spin state of the Fe(III)N_4 moieties. The $Ti_3C_2Br_x$/FePc composite, with 88.1% of its iron in the intermediate spin state, exhibited superior electrochemical performance, achieving an ORR half-wave potential of 0.94 V versus RHE. This represents a substantial improvement over the low-spin state FePc catalyst.

Moreover, the $Ti_3C_2Br_x$/FePc catalyst demonstrated a remarkable increase in power densities, reaching 252.5 mW cm^{-2} in ZAB batteries and 350.7 mW cm^{-2} in AEMFC H_2-O_2 fuel cells, effectively doubling the performance compared to the pristine FePc catalyst. These improvements underscore the pivotal role of the intermediate spin state in enhancing ORR efficiency and provide a clear correlation between spin state transitions and catalytic performance.

Through a combination of experimental analysis and density functional theory (DFT) studies, we elucidated the underlying mechanisms contributing to this enhanced activity. The intermediate spin state promotes electron filling in the anti-bonding orbital composed of Fe $3dz^2$ and O_2 π^* orbitals, facilitating more effective O_2 activation and optimizing the ORR pathway. Our comprehensive approach not only advances the understanding of the spin-activity relationship in ORR catalysis but also highlights the potential of spin state engineering in the design of high-performance, non-precious metal ORR catalysts.

AUTHOR INFORMATION

Corresponding Author

* Corresponding Author

Genban Sun −*Beijing Key Laboratory of Energy Conversion and Storage Materials Institution, College of Chemistry, Beijing Normal University, Beijing 100875, China; orcid.org/0000-0001-9005- 8123; Email: gbsun@bnu.edu.cn*

Authors

Shuren Zhang − *Beijing Key Laboratory of Energy Conversion and Storage Materials Institution, College of Chemistry, Beijing Normal University, Beijing 100875, China; orcid.org/ 0000-0002-1530-298X; Email: zhangshuren@bnu.edu.cn*

Author Contributions

The manuscript was written through contributions of all authors. All authors have given approval to the final version of the manuscript.

Notes

The authors declare no competing financial interest.

ACKNOWLEDGMENT

This project was supported by the National Natural Science Foundation of China [Nos: 22271018]

REFERENCES

1. Zhang Z, Feng C, Wang D, Zhou S, Wang R, Hu S*, et al.* Selectively anchoring single atoms on specific sites of supports for improved oxygen evolution. *Nature Communications* 2022, **13**(1)**:** 2473.

2. Chattot R, Le Bacq O, Beermann V, Kühl S, Herranz J, Henning S*, et al.* Surface distortion as a unifying concept and descriptor in oxygen reduction reaction electrocatalysis. *Nature Materials* 2018, **17**(9)**:** 827-833.

3. Yang G, Zhu J, Yuan P, Hu Y, Qu G, Lu B-A*, et al.* Regulating Fe-spin state by atomically dispersed Mn-N in Fe-N-C catalysts with high oxygen reduction activity. *Nature Communications* 2021, **12**(1)**:** 1734.

4. Chen C, Tang Z-J, Li J-Y, Du C-Y, Ouyang T, Xiao K*, et al.* MnO Enabling Highly Efficient and Stable Co-Nx/C for Oxygen Reduction Reaction in both Acidic and Alkaline Media. *Advanced Functional Materials* 2023, **33**(1)**:** 2210143.

5. Shin H, Kim H-i, Chung DY, Yoo JM, Weon S, Choi W*, et al.* Scaffold-Like Titanium Nitride Nanotubes with a Highly Conductive Porous Architecture as a Nanoparticle Catalyst Support for Oxygen Reduction. *ACS Catalysis* 2016, **6**(6)**:** 3914-3920.

6. Yang S, Tak YJ, Kim J, Soon A, Lee H. Support Effects in Single-Atom Platinum Catalysts for Electrochemical Oxygen Reduction. *ACS Catalysis* 2017, **7**(2)**:** 1301-1307.

7. Li J, Chen M, Cullen DA, Hwang S, Wang M, Li B*, et al.* Atomically dispersed manganese catalysts for oxygen reduction in proton-exchange membrane fuel cells. *Nature Catalysis* 2018, **1**(12)**:** 935-945.

8. Wan X, Liu X, Li Y, Yu R, Zheng L, Yan W*, et al.* Fe–N–C electrocatalyst with dense active sites and efficient mass transport for high-performance proton exchange membrane fuel cells. *Nature Catalysis* 2019, **2**(3)**:** 259-268.

9. Li Z, Zhuang Z, Lv F, Zhu H, Zhou L, Luo M*, et al.* The Marriage of the FeN4 Moiety and MXene Boosts Oxygen Reduction Catalysis: Fe 3d Electron Delocalization Matters. *Advanced Materials* 2018, **30**(43)**:** 1803220.

10. Marshall-Roth T, Libretto NJ, Wrobel AT, Anderton KJ, Pegis ML, Ricke ND*, et al.* A pyridinic Fe-N4 macrocycle models the active sites in Fe/N-doped carbon electrocatalysts. *Nature Communications* 2020, **11**(1)**:** 5283.

11. Lu F, Fan K, Cui L, Li B, Yang Y, Zong L*, et al.* Engineering FeN4 active sites onto nitrogen-rich carbon with tubular channels for enhanced oxygen reduction reaction performance. *Applied Catalysis B: Environmental* 2022, **313:** 121464.

12. Han A, Wang X, Tang K, Zhang Z, Ye C, Kong K*, et al.* An Adjacent Atomic Platinum Site Enables Single-Atom Iron with High Oxygen Reduction Reaction Performance. *Angewandte Chemie International Edition* 2021, **60**(35)**:** 19262-19271.

13. Li Y, Liu X, Zheng L, Shang J, Wan X, Hu R*, et al.* Preparation of Fe－N－C catalysts with FeNx (x = 1, 3, 4) active sites and comparison of their activities for the oxygen reduction reaction and performances in proton exchange membrane fuel cells. *Journal of Materials Chemistry A* 2019, **7**(45)**:** 26147-26153.

14. Han Y, Wang Y-G, Chen W, Xu R, Zheng L, Zhang J*, et al.* Hollow N-Doped Carbon Spheres with Isolated Cobalt Single Atomic Sites: Superior Electrocatalysts for Oxygen Reduction. *Journal of the American Chemical Society* 2017, **139**(48)**:** 17269-17272.

15. Zhao Y, Chen H-C, Ma X, Li J, Yuan Q, Zhang P*, et al.* Vacancy Defects Inductive Effect of Asymmetrically Coordinated Single-Atom Fe—N3S1 Active Sites for Robust Electrocatalytic Oxygen Reduction with High Turnover Frequency and Mass Activity. *Advanced Materials* 2024, **36**(11)**:** 2308243.

16. Wang X, Jia Y, Mao X, Liu D, He W, Li J*, et al.* Edge-Rich Fe−N4 Active Sites in Defective Carbon for Oxygen Reduction Catalysis. *Advanced Materials* 2020, **32**(16)**:** 2000966.

17. Sun S, Zhang Y, Shi X, Sun W, Felser C, Li W*, et al.* From Charge to Spin: An In-Depth Exploration of Electron Transfer in Energy Electrocatalysis. *Advanced Materials*, **n/a**(n/a)**:** 2312524.

18. Dai Y, Liu B, Zhang Z, Guo P, Liu C, Zhang Y*, et al.* Tailoring the d-Orbital Splitting Manner of Single Atomic Sites for Enhanced Oxygen Reduction. *Advanced Materials* 2023, **35**(14)**:** 2210757.

19. Liu Y, Liu X, Lv Z, Liu R, Li L, Wang J*, et al.* Tuning the Spin State of the Iron Center by Bridge-Bonded Fe-O-Ti Ligands for Enhanced Oxygen Reduction. *Angewandte Chemie International Edition* 2022, **61**(21)**:** e202117617.

20. Zhao K-M, Liu S, Li Y-Y, Wei X, Ye G, Zhu W*, et al.* Insight into the Mechanism of Axial Ligands Regulating the Catalytic Activity of Fe－N4 Sites for Oxygen Reduction Reaction. *Advanced Energy Materials* 2022, **12**(11)**:** 2103588.

21. Wang Y, Meng P, Yang Z, Jiang M, Yang J, Li H*, et al.* Regulation of Atomic Fe-Spin State by Crystal Field and Magnetic Field for Enhanced Oxygen Electrocatalysis in Rechargeable Zinc-Air Batteries. *Angewandte Chemie International Edition* 2023, **62**(28)**:** e202304229.

22. Mugiraneza S, Hallas AM. Tutorial: a beginner’s guide to interpreting magnetic susceptibility data with the Curie-Weiss law. *Communications Physics* 2022, **5**(1)**:** 95.

23. Li M, Li X, Qin G, Luo K, Lu J, Li Y*, et al.* Halogenated Ti3C2 MXenes with Electrochemically Active Terminals for High-Performance Zinc Ion Batteries. *ACS Nano* 2021, **15**(1)**:** 1077-1085.

24. Chen J, Jin Q, Li Y, Shao H, Liu P, Liu Y*, et al.* Molten Salt-Shielded Synthesis (MS3) of MXenes in Air. *ENERGY & ENVIRONMENTAL MATERIALS* 2023, **6**(2)**:** e12328.

25. Gong S, Zhao F, Xu H, Li M, Qi J, Wang H*, et al.* Iodine-Functionalized Titanium Carbide MXene with Ultra-Stable Pseudocapacitor Performance. *Journal of Colloid and Interface Science* 2022, **615:** 643-649.

26. Liu P, Xiao P, Lu M, Wang H, Jin N, Lin Z. Lithium storage properties of Ti3C2Tx (Tx = F, Cl, Br) MXenes. *Chinese Chemical Letters* 2023, **34**(4)**:** 107426.

27. Hou T, Luo Q, Li Q, Zu H, Cui P, Chen S*, et al.* Modulating oxygen coverage of Ti3C2Tx MXenes to boost catalytic activity for HCOOH dehydrogenation. *Nature Communications* 2020, **11**(1)**:** 4251.

28. Ma L, Jiang Y-K, Xu D-R, Fang Y-Y, Li N, Cao D-Y*, et al.* Enabling Stable and Low-Strain Lithium Plating/Stripping with 2D Layered Transition Metal Carbides by Forming Li-Zipped MXenes and a Li Halide-Rich Solid Electrolyte Interphase. *Angewandte Chemie International Edition* 2024, **63**(13)**:** e202318721.

29. Li Y, Shao H, Lin Z, Lu J, Liu L, Duployer B*, et al.* A general Lewis acidic etching route for preparing MXenes with enhanced electrochemical performance in non-aqueous electrolyte. *Nature Materials* 2020, **19**(8)**:** 894-899.

30. Dash A, Vaßen R, Guillon O, Gonzalez-Julian J. Molten salt shielded synthesis of oxidation prone materials in air. *Nature Materials* 2019, **18**(5)**:** 465-470.

31. Chen K, Liu K, An P, Li H, Lin Y, Hu J*, et al.* Iron phthalocyanine with coordination induced electronic localization to boost oxygen reduction reaction. *Nature Communications* 2020, **11**(1)**:** 4173.

32. Sun Y, Sun S, Yang H, Xi S, Gracia J, Xu ZJ. Spin-Related Electron Transfer and Orbital Interactions in Oxygen Electrocatalysis. *Advanced Materials* 2020, **32**(39)**:** 2003297.

33. Kennedy BJ, Murray KS, Zwack PR, Homborg H, Kalz W. Spin states in iron(III) phthalocyanines studied by Moessbauer, magnetic susceptibility, and ESR measurements. *Inorganic Chemistry* 1986, **25**(15)**:** 2539-2545.

34. Zeng Y, Li X, Wang J, Sougrati MT, Huang Y, Zhang T*, et al.* In situ/operando Mössbauer spectroscopy for probing heterogeneous catalysis. *Chem Catalysis* 2021, **1**(6)**:** 1215-1233.

35. Li X, Cao C-S, Hung S-F, Lu Y-R, Cai W, Rykov AI*, et al.* Identification of the Electronic and Structural Dynamics of Catalytic Centers in Single-Fe-Atom Material. *Chem* 2020, **6**(12)**:** 3440-3454.

36. Lin L, Xu Y, Han Y, Xu R, Wang T, Sun Z*, et al.* Spin-Magnetic Effect of d-π Conjugation Polymer Enhanced O−H Cleavage in Water Oxidation. *Journal of the American Chemical Society* 2024.

37. Lin F, Guo S. Defect-modulated O-coordination: A new strategy for electronic structure two-tier tuning. *Chem Catalysis* 2022, **2**(4)**:** 650-653.

38. Wang R, Zhang L, Shan J, Yang Y, Lee J-F, Chen T-Y*, et al.* Tuning Fe Spin Moment in Fe–N–C Catalysts to Climb the Activity Volcano via a Local Geometric Distortion Strategy. *Advanced Science* 2022, **9**(31)**:** 2203917.

39. Liu K, Fu J, Lin Y, Luo T, Ni G, Li H*, et al.* Insights into the activity of single-atom Fe-N-C catalysts for oxygen reduction reaction. *Nature Communications* 2022, **13**(1)**:** 2075.